Nano Energy 136 (2025) 110757

Contents lists available at ScienceDirect

Nano Energy

journal homepage: www.elsevier.com/locate/nanoen

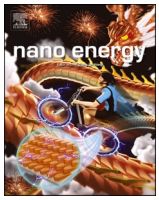

Full paper

Fully self-healing dual-mode tactile sensing strategy for object's dimension and surface morphology recognition

Xuanzi Luo [a,1], Xin Zhang [a,1], Shanpeng Ji [a], Chao Wu [a], Lin Cheng [a,*], Daoyou Guo [a], Shunli Wang [a], Huaping Wu [b,*], Aiping Liu [a,*]

[a] Zhejiang Key Laboratory of Quantum State Control and Optical Field Manipulation, Department of Physics, Zhejiang Sci-Tech University, Hangzhou 310018, China
[b] Key Laboratory of Special Purpose Equipment and Advanced Processing Technology, Ministry of Education and Zhejiang Province, College of Mechanical Engineering, Zhejiang University of Technology, Hangzhou 310023, China

ARTICLE INFO

Keywords:
Dual-mode tactile sensing strategy
Self-healing
Dimension recognition
Surface morphology recognition
Hydrogen bond

ABSTRACT

Bionic flexible tactile sensors have emerged as a popular solution for emulating the human hand's tactile system in wearable devices and smart robots. However, achieving durability and resistance to disruption while enhancing tactile sensing capabilities remains a critical challenge. In this study, we propose a dual-mode tactile sensing strategy with comprehensive self-healing capabilities, combining piezoresistive and piezoelectric sensing to accurately simulate finger bending and touching motions for perception of dynamic and static stimuli. Especially, we introduce an infusive polydimethylsiloxane (H-PDMS) material with self-healing function as the key component of our tactile sensing system, enabling rapid recovery after damage similar to the self-healing ability of human skin. The size of the object is recognized by the liquid metal-based piezoresistive sensor to mimic changes in finger joint bending, while the contour of the object's surface is recognized by the ceramic nanoparticle-included piezoelectric sensor to simulate the tactile receptors of the finger. During object recognition, signals from both sensors are converted into CMYK color blocks and superimposed, enabling accurate discrimination of object size and surface characteristics. Remarkably, the sensing system achieves a comprehensive recognition rate of 96 %, even under damaged conditions, with a self-healing rate in electrical conductivity and sensing capabilities exceeding 90 %. This exceptional self-healing performance is driven by the abundant hydrogen bonds of varying strengths within the H-PDMS matrix, which enable the material to recover its original properties following damage. By introducing this self-healing functionality into electronic skin technology, our work paves the way for advanced applications, including robotic object recognition and automated fruit sorting, offering broad prospects for smart systems in various industries.

1. Introduction

Fingers serve as the primary means through which humans physically engage with the external environment [1], perceiving attributes such as shape, material and temperature of an object via touch [2,3]. This perception relies on subtle deformations that occur in the finger skin upon contact with an object, thereby providing accurate tactile feedback [4–6]. This intricate perceptual process plays a pivotal role in various aspects of human daily life and fine manipulation tasks, encompassing essential functions like object classification, surface quality assessment, and precision manipulation [7–10]. With the rapid development of human-computer interaction technology, intelligent sensing systems and bionic robotics, researchers are increasingly directing their attention towards developing bionic flexible tactile sensors [11,12]. These sensors not only emulate the tactile capabilities of human fingers, but also possess flexible, stretchable, and self-healing characteristics that render them suitable for diverse complex applications.

Bionic flexible tactile sensors encompass both dynamic and static pressure sensing in the recognition of objects [13–15]. Static signals typically reflect continuously applied forces, providing information about the shape or position of the object in contact with the sensor, while dynamic signals correspond to instantaneous or changing forces, reflecting the sliding characteristics of the object or surface roughness.

* Corresponding authors.
E-mail addresses: chenglin@zstu.edu.cn (L. Cheng), wuhuaping@gmail.com (H. Wu), liuaiping1979@gmail.com (A. Liu).
[1] Authors contribute equally

https://doi.org/10.1016/j.nanoen.2025.110757
Received 28 December 2024; Received in revised form 25 January 2025; Accepted 5 February 2025
Available online 6 February 2025

The integration of dynamic and static signals is critical in achieving accurate tactile recognition [16–20]. By combining these two signal types, flexible dual-mode tactile sensors with piezoresistive-piezoelectric effects significantly enhance detection accuracy and reliability [21–24], aiming at perceiving both dynamic and static aspects. For example, Dan et al. proposed a distributed hand tactile sensor that employed a combination of polyvinylidene fluoride (PVDF) piezoelectric membrane and carbon nanotube/polymer composite piezoresistive membrane to achieve dual sensing functionality for both dynamic and static forces [25]. Similarly, Gao et al. designed a sensor by combining piezoresistive hydrogel and PVDF film which successfully captured the dimensional and contour signals of an object, thereby improving the recognition accuracy [26]. In addition, Lee et al. developed a haptic sensor primarily composed of silver and ZnO nanowires possessing various electrical properties such as piezoelectricity, frictionality, and piezoresistivity; integrating these haptic sensors into a robot enabled material identification as well as texture discrimination capabilities [27]. However, despite their exceptional performance in dynamic and static signal detection, dual-mode sensors are vulnerable to damage in practical applications due to multiple tension and compression deformations. They may experience performance degradation caused by fatigue or accidental damage during prolonged use or high-frequency

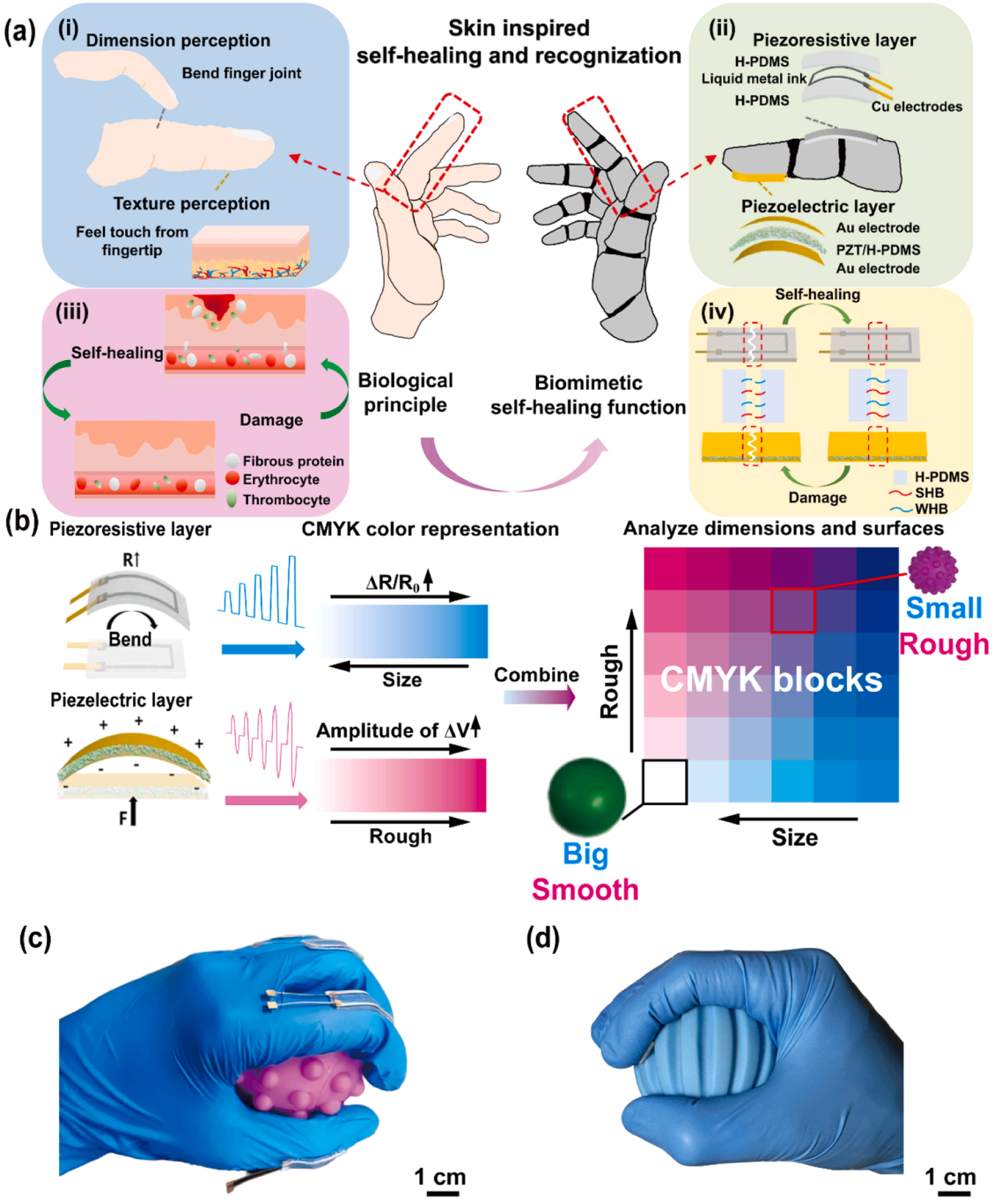

Fig. 1. Structure and function of the fully self-healing tactile sensing system. (a) The correspondence between recognition and self-healing function of sensor and human finger: (i) different parts role of human fingers in recognizing objects; (ii) installation method of the sensors and their structure; (iii) self-healing mechanism of human skin; (iv) self-healing mechanism of sensor. (b) Flow chart using CMYK color block notation to detect object size and surface morphology. (c) Optical image of piezoresistive sensors worn on the fingers of a volunteer. (d) Optical image of piezoelectric sensors worn on the fingers of a volunteer.

contact scenarios. In contrast, human skin possesses a natural self-healing function that enables gradual recover of its original sensing ability even when punctured by sharp objects [28]. This self-healing ability significantly enhances fault tolerance during object recognition in complex environments [29–31]. Integrating self-healing materials into flexible sensors represents a significant breakthrough in the development of bionic electronic skin [32–34]. For instance, Bao et al. successfully incorporated self-healing capabilities into a robot's electronic skin via grafting hydrogen bonds in polydimethylsiloxane (PDMS), thereby enhancing the device's durability and reliability [35]. Huang et al. also utilized hydrogen bonds to introduce self-power sensing ability and efficient dynamic sensing capability into PDMS-based materials for sensor fabrication [36]. Zhang et al., on the other hand, synthesized a self-powered electronic skin sensor capable of detecting bending and pressure signals by introducing disulfide and hydrogen bonds into a polyurethane chain [37]. However, the majority of current research centers on single-mode self-healing sensors that are limited to reconstruct either dynamic or static sensing capabilities after damage, but not both simultaneously. Therefore, it is imperative to investigate the integration of multi-mode sensing signals with comprehensive self-healing properties in electronic skin research.

Inspired by the tactile perception of humans grasping objects with their hands (Fig. 1a(i)), this study presents a flexible dual-mode tactile sensing system that leverages piezoresistive and piezoelectric effects to achieve high sensitivity and accuracy in dynamic-static perception and object recognition (Fig. 1a(ii)). For human skin, thrombocytes and fibrous protein cells play a crucial role in assisting the self-healing process of the skin (Fig. 1a(iii)) [38]. Drawing inspiration from the healing function of human skin, we introduce a self-healable polydimethylsiloxane (H-PDMS) material, rich in hydrogen bonds, as the core component for constructing tactile sensing system with complete self-healing capabilities and exceptional durability. The self-healing mechanism of H-PDMS is driven by the interplay of strong hydrogen bonds (SHBs) and weak hydrogen bonds (WHBs), which enable efficient recovery of force/deformation, electrical conduction, and sensing performance, closely mimicking the functionality of human skin (Fig. 1a (iv)). Furthermore, we employ the CMYK color block superposition principle to comprehensively represent the combined recognition results from the dual-mode sensing system, capturing object size and surface roughness (Fig. 1b). This dual-mode tactile sensing strategy is successfully implemented with a robotic arm to sort lychee quality in agricultural applications. This demonstrates its significant potential for use in electronic skin, bionic robotics, and automated fruit sorting, marking a substantial advancement in tactile sensing technologies.

2. Experimental section

2.1. Preparation of self-healing H-PDMS

Firstly, a mixture of 10 g aminopropyl terminated polydimethylsiloxane (AT-PDMS) and 0.70 g triethylamine (TEA) were added to 100 mL dichloromethane (CH_2Cl_2), followed by thorough mixing in an ice water bath for 1 h. Subsequently, the mixture was combined with 0.31 g of 4,4 '-methylene bis (cyclohexyl isocyanate) (HMDI) and 0.18 g of isophorone diisocyanate (IPDI) in an ice water bath under a nitrogen atmosphere for another hour. The reaction was restored to room temperature and continued for a duration of 24 h. Finally, the resulting solution of polydimethylsiloxane with self-healing function (H-PDMS) was obtained.

2.2. Preparation of self-healing liquid metal ink

Firstly, 0.50 g of liquid metal was introduced in 100 mL solution of CH_2Cl_2 containing 10 g of H-PDMS for initial mixing. The resulting mixture was then subjected to crushing using a cell crusher operating at a power of 550 W for a duration of 1 h. Subsequently, the crushed solution underwent centrifugation at a speed of 8000 rpm for 5 min using a high-speed centrifuge. A distinct stratification of mixed solution was observed with the lower sediment representing the self-healing liquid metal ink (Fig. S1).

2.3. Fabrication of self-healing piezoresistive sensor

The H-PDMS solution was first poured into a polytetrafluoroethylene (PTFE) mold with dimensions of 25 mm× 10 mm× 5 mm, and then the mold was transferred to an oven at 60℃ for 2 h to obtain a transparent H-PDMS substrate. Following this, "U" shaped grooves were engraved onto a polyimide film (PI) using UV cutting technology and placed onto the aforementioned piece of H-PDMS substrate as mask plate guide lines. Liquid metal ink was uniformly applied within these "U" grooves before removing the mask plate upon completion. Copper foil electrodes were connected to both ends as lead wires for electrical connection purposes. Finally, another piece of H-PDMS material was coated with liquid metal ink and left at room temperature for approximately 24 h to facilitate self-healing between two pieces of H-PDMS layers to form an integrated package structure (Fig. S2). The optical diagram of the fabricated self-healing piezoresistive sensors worn on the fingers of a volunteer is shown in Fig. 1c.

2.4. Modification of ceramic nanoparticles

Surface modification was necessary for lead zirconate titanate (PZT) particles to minimize agglomeration before composite formation with H-PDMS. The surface modification process involved immersing the PZT particles in an ethanol solution, followed by ball milling using a planetary ball mill for 24 h to reduce particle diameter. Subsequently, the PZT particles were dried in an oven for 12 h to remove the ethanol. Next, the PZT particles were subjected to sonication in hydrogen peroxide for 2 h and thoroughly washed with deionized water. Then, an ethanol solution containing 3 % v/v acid propyl ester (TMSPM) was added and after sufficient mixing at room temperature for 5 h, the PZT particles were filtered out, washed again with deionized water, and finally dried in an oven at 60℃ for 12 h.

2.5. Fabrication of self-healing piezoelectric sensor

To prepare the piezoelectric sensor, 5 g of modified PZT powder was dispersed in a mixture of CH_2Cl_2 (100 mL) and H-PDMS (10 g) using ultrasonic processing, followed by stirring with a magnetic stirrer until achieving homogeneity. The resulting mixture was poured into a PTFE mold measuring 10 mm× 10 mm× 2 mm and cured to obtain the piezoelectric composite film. This film was then placed between positive and negative plates of a high-voltage electric field setup where the intensity of electric field gradually increased from zero to 4 kV/mm over half-hour intervals until polarization completion after holding it steady for another two hours. After that, any remaining silicon oil on the surface of the piezoelectric film was wiped off using ethanol as solvent. Finally, gold electrodes were plated on both sides of the composite film through magnetron sputtering technique, resulting in a self-healing piezoelectric film containing 50 wt% PZT particles (Fig. S3). The optical diagram of the fabricated self-healing piezoelectric sensors worn on the fingers of a volunteer is shown in Fig. 1d.

2.6. Measurement and characterization

The Fourier transform infrared spectroscopy (FT-IR) was conducted in the range of 500–4000 cm^{-1} using a Fourier infrared spectrometer (Nicolet™ iS50, Thermo Scientific™). Both microscopic morphology and elemental distribution were obtained by scanning electron microscopy (SEM, CARL ZEISS SMT PTE Ltd.), where the microscopic images were obtained under high voltage conditions at 3 kV and the elemental distribution maps were obtained under high voltage at 10 kV. The

mechanical properties of the materials were characterized using a mechanical testing machine (HY-0230, Yiheng Precision Instruments). The piezoresistive signal output was measured by Keithley-2400 SourceMeter. The piezoelectric signal output was measured by KSI-8103 charge amplifier and data acquisition card (USB_HRF4028, Heng rui feng Measurement and Control Technology Co., Ltd.).

3. Results and discussion

3.1. Self-healable H-PDMS characteristic

The proposed sensor utilizes H-PDMS with self-healable ability as the substrate, which possesses self-repairing properties and endows the sensor with a function similar to human skin. The infrared spectra of H-PDMS and AT-PDMS are shown in Fig. S4, where the characteristic peaks of urethane amide I and amide II for H-PDMS appear at approximately 1629 cm^{-1} and 1566 cm^{-1} , respectively. The peak observed in the urethane amide I region mainly stems from the stretching vibration of the carbonyl group (C═O) and the stretching and deformation vibration of the isocyanate group (-NCO), which proves evidence for successful reaction between AT-PDMS and IPDI, and hydrogen bond synthesis. In this type of hydrogen bonding, due to steric hindrance imposed by IPDI, IPDI can only form a double hydrogen bond with another IPDI unit [39], referred to as WHB, corresponding to the (W-H) component depicted in Fig. 2a and Fig. S4. In addition, the vibration of urethane amide II region is a combination of N-H plane bending vibration and C-N stretching vibration, typically occurring between 1565 and 1570 cm^{-1}. In this work, a characteristic peak of urethane amide II appeared at 1566 cm^{-1} in the infrared spectrograms of H-PDMS is also a typical characteristic region of N-H•••Y type hydrogen bond system [40]. Due to its symmetric structure, HMDI can form a quadruple hydrogen bond with the inverted HMDI structure [41], known as SHB, corresponding to the (S-H) component in Fig. 2a and Fig. S4. The infrared spectra prove the fact that the successful grafting of IPDI and HMDI on AT-PDMS provide two different hydrogen bonds for the material. Specifically, the SHB formed by HMDI is a stronger quadruple hydrogen bond compared to the WHB formed by IPDI, providing better elasticity to the material. On the other hand, WHB acts as sacrificial bonds provided by IPDI that dissipate strain energy through effective reversible breaking and recombination processes, thereby improving material circular availability and durability [35,42].

During the self-healing process, H-PDMS undergoes self-repair via non-dynamic covalent bonds facilitated by its intrinsic hydrogen bond network (as illustrated in Fig. 2b). Upon damage, hydrogen bonds

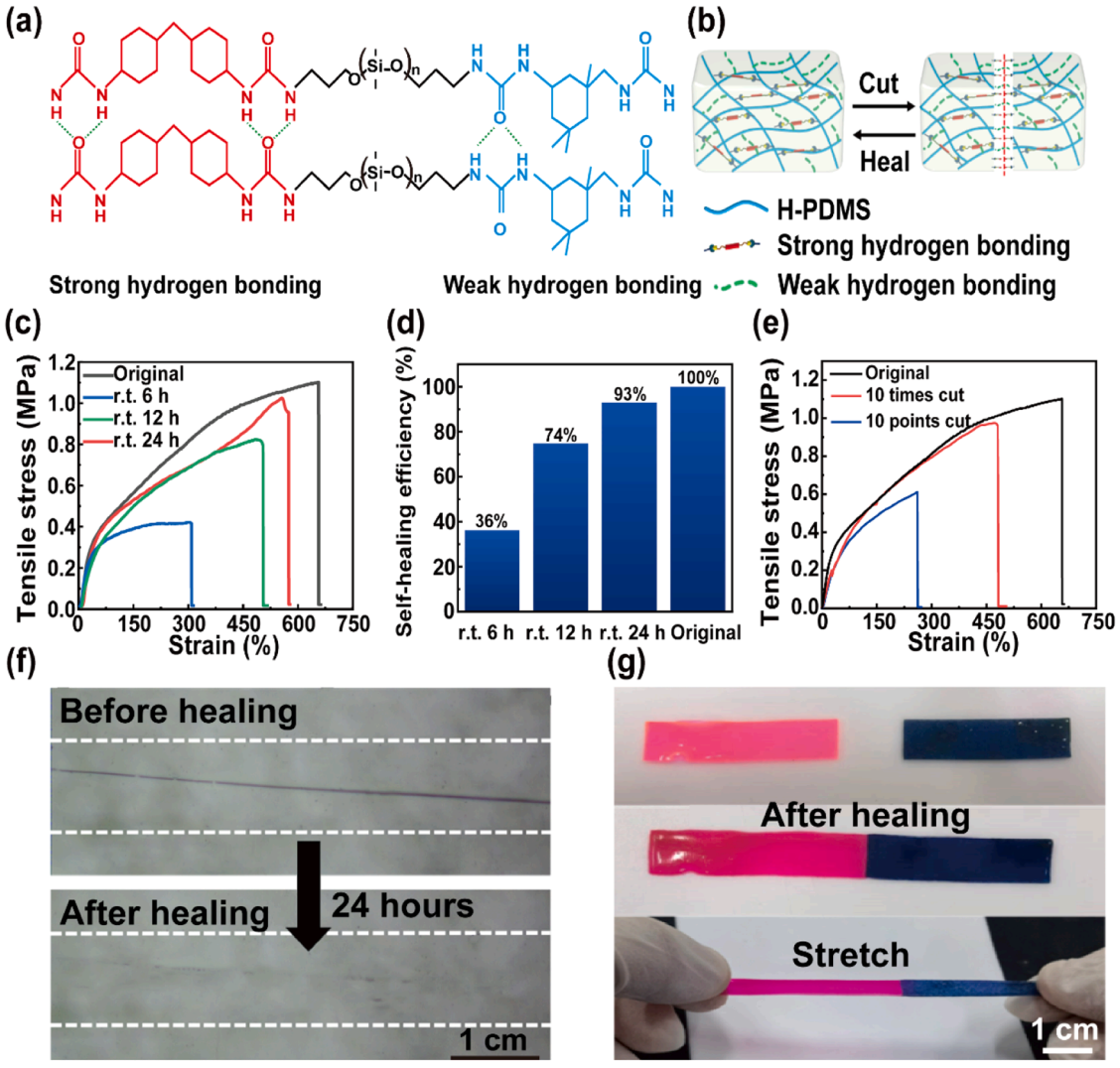

Fig. 2. Principle and characteristics of self-healing H-PDMS substrate. (a) The formula of strong and weak hydrogen bonds. (b) Self-healing principle of H-PDMS. (c) Comparison of mechanical properties of H-PDMS before and after self-healing. (d) Self-healing efficiency of H-PDMS after different self-repair conditions. (e) Mechanical properties of H-PDMS after 10-time and 10-point cutting methods. (f) Optical microscope images of H-PDMS before and after self-healing after knife incision. (g) Two pieces of self-healing H-PDMS were placed together to form a self-healable connection between these two pieces of H-PDMS.

reform between the contact surfaces at the fracture site due to the movement of molecular chains, thereby reintegrating the fractured material. We investigate the impact of varying SHB and WHB content (achieved by adjusting the molar ratios of HMDI and IPDI during H-PDMS synthesis) on the mechanical and self-healing properties of H-PDMS. Specifically, four groups of H-PDMS with different compositions were prepared using HMDI to IPDI molar ratios ranging from 2:8–8:2, and their tensile stress-strain behavior and self-healing efficiency at room temperature (r.t.) condition were evaluated. The samples with the dimensions of 25 mm× 10 mm× 1 mm were denoted as $HMDI_2$-$IPDI_8$, $HMDI_4$-$IPDI_6$, $HMDI_6$-$IPDI_4$, and $HMDI_8$-$IPDI_2$, respectively, according to the molar ratio of HMDI to IPDI. As shown in Fig. S5a, the deformation of the four different H-PDMS compositions exceeds 600 %, with $HMDI_6$-$IPDI_4$ and $HMDI_8$-$IPDI_2$ reaching 660 % and 664 %, respectively. With increasing HMDI content in H-PDMS, the proportion of SHB in the material also increases, enhancing the material's stability and elasticity, and consequently, its tensile strength and elongation at break. When H-PDMS was synthesized with $HMDI_6$-$IPDI_4$ and $HMDI_8$-$IPDI_2$ ratios, the ultimate tensile stress of H-PDMS reaches 1.10 MPa and 1.12 MPa, respectively. The self-healing efficiency of H-PDMS material was calculated using the equation $\eta = P_{Healed}/P_{Original}$ (where $P_{Original}$ and P_{Healed} represent the tensile stress of H-PDMS before and after self-healing, respectively). After cutting the H-PDMS materials under r.t. condition and allowing them to self-heal for 24 h, tensile stress-strain experiments were conducted. The results reveal that the self-healing efficiency of all four groups exceed 80 %, with the $HMDI_6$-$IPDI_4$ ratio achieving the highest efficiency of 93 % (Fig. S5b). Consequently, the molar ratio of $HMDI_6$-$IPDI_4$ was selected for the preparation of H-PDMS in subsequent experiments.

To investigate the effect of self-healing time on the mechanical properties and self-healing efficiency of H-PDMS, the midsection of the material was cut, and the fractured surfaces of the two pieces were brought into contact to heal at r.t. condition for different durations. The results indicate that self-healing time has a significant impact on both the mechanical properties and self-healing efficiency of H-PDMS (Fig. 2c). When the damaged H-PDMS is allowed to self-heal for 6 h, 12 h and 24 h, the ultimate tensile deformation and ultimate tensile stress reach 305 % and 0.40 MPa (6 h), 491 % and 0.81 MPa (12 h), 580 % and 1.02 MPa (24 h), respectively. The corresponding self-healing efficiencies for these time periods are illustrated in Fig. 2d, indicating a gradual self-healing process. Notably, the material achieves a high self-repair efficiency of 93 % within just 24 h, ensuring rapid recovery of its original mechanical properties post-damage. This is attributed to the participation of IPDI in WHB formation during self-healing, which facilitates faster healing rates. After self-healing, SHBs provided by HMDI offer superior elasticity and toughness compared to WHBs, thereby enhancing the overall mechanical properties [35]. The self-repair process of H-PDMS was observed using the cut-contact method (Fig. 2f), wherein the incised traces vanish completely after a duration of 24 h at r.t. condition, demonstrating the excellent self-repair capability of H-PDMS in the cut mode. To enhance visualization, two pieces of H-PDMS were stained and subsequently brought into contact on a common horizontal plane. After 24-h self-repair process, the two pieces of H-PDMS fuse into a single piece, which could be manually stretched by hand (Fig. 2g). These experiments further demonstrate the excellent self-repairing ability of H-PDMS in the contact mode, making it an excellent substrate material for self-repairing sensors. However, when H-PDMS undergoes simultaneous damage-recovery at 10 positions, the tensile stress recovers to 0.58 MPa with a self-repair efficiency of 53 %. This reduction in efficiency can be attributed to the inherent challenges of performing in-situ self-repair at multiple damaged locations simultaneously, resulting in a significant decrease in the material's mechanical properties. Nevertheless, when subjected to 10 cycles of cutting and subsequent self-repairing at the same location, the tensile stress recovers to 0.97 MPa with a self-repairing efficiency of 88 %, nearly matching the performance observed after a single damage event (Fig. 2e). This is due to the spontaneous nature of an electrostatic force for hydrogen bonding, which requires no external energy input for bond formation [40]. This characteristic indicates that H-PDMS has the capability for repeated self-healing.

3.2. Sensing performance of self-healable piezoresistive sensor

The sensing performance evaluation of the flexible piezoresistive sensor was conducted utilizing liquid metal self-healing ink as the conductor along with H-PDMS as the self-healable matrix material. As shown in Fig. S6a, the liquid metal exhibits surface tension in its normal state, making it challenging to spread and unfold on the H-PDMS film. The SEM image in Fig. S6b reveals that the liquid metal droplets are isolated and non-uniformly distributed under normal conditions. This behavior is primarily attributed to the presence of an oxide layer on the droplet surface, which restricts the mobility of the liquid metal and impedes its effective spreading on the substrate. After forming self-healing liquid metal ink, however, the ink spreads well on H-PDMS and can be patterned into various forms using a mask plate (Fig. S6c). The SEM image in Fig. S6d reveals that the grinder-processed small particles of liquid metal can bond through H-PDMS to form evenly distributed larger ink particles, enabling the ink to be shaped into different configurations.

To evaluate the sensing performance of piezoresistive sensor, we analyzed its linearity (R^2) and sensitivity factor ($SFR = (\Delta R/R_0)/\Delta\theta$), where ΔR represents the change in resistance, R_0 is the initial resistance value, and $\Delta\theta$ denotes the change in bending angle. During bending tests within 0–90° range, the sensor's resistance change exhibits a nearly linear relationship with the bending angle ($R^2 = 0.98$), resulting in a SFR of 0.2 (Fig. 3a). When applied to the finger joint bending test, the self-healing piezoresistive sensor displays sensitivity by showing resistance changes of 4 %, 10 %, and 15 % at bending angles of 30°, 60°, and 90° (Fig. 3b), respectively. Notably, after intentional cutting the sensor in half and allowing it to self-heal at r. t. condition for 24 h, the stability and consistency of resistance measurements before damage and after healing remain unaffected during another round of finger joint bending tests (Fig. 3b), highlighting the excellent self-healing capability of this sensor. Since the piezoresistive sensor uses H-PDMS as both the substrate and packaging material, its self-healing mechanism aligns with that of H-PDMS, requiring 24 h for mechanical property recovery. However, the electrical signal recovery time of the sensor is significantly shorter than the mechanical property recovery time. Owing to the conductive nature of the liquid metal ink utilized in piezoresistive sensors, free electrons within the material form a conductive pathway. Upon sensor damage, when the two broken ends come into contact, free electrons rapidly move between them, re-establishing the conductive path almost instantaneously [43]. Experimental results show that the electrical signal of the piezoresistive sensor is restored within 150 ms during the self-healing process (Fig. 3c). Further evidence supporting this characteristic is presented in Fig. S7, whereupon contacting the broken ends of the damaged sensor leads to immediate resumption of LED illumination due to its rapid self-healing capability. This swift recovery in conductivity ensures prompt restoration of conductive functionality following destruction. Moreover, after undergoing 24 h of self-healing, piezoresistive sensors were subjected to an experimental bending test involving 1000 cycles at a 90° angle; results depicted in Fig. 3d demonstrate that this self-repaired sensor exhibits commendable stability and repeatability in terms of their electrical sensing signals. Additionally, five instances of cutting and subsequent self-repair were performed on these sensors (Fig. 3e and f), with resistance values and repair capabilities remaining consistent across multiple cycles with an initial resistance change approximately equaling 5 %. Consequently, the self-healing efficiency of the sensing signal reaches 95 %. These findings indicate that even after repeated cuts and self-repair cycles, these piezoresistive sensors maintain effective sensing performance and demonstrate potential for long-term utilization. In addition to the mechanical

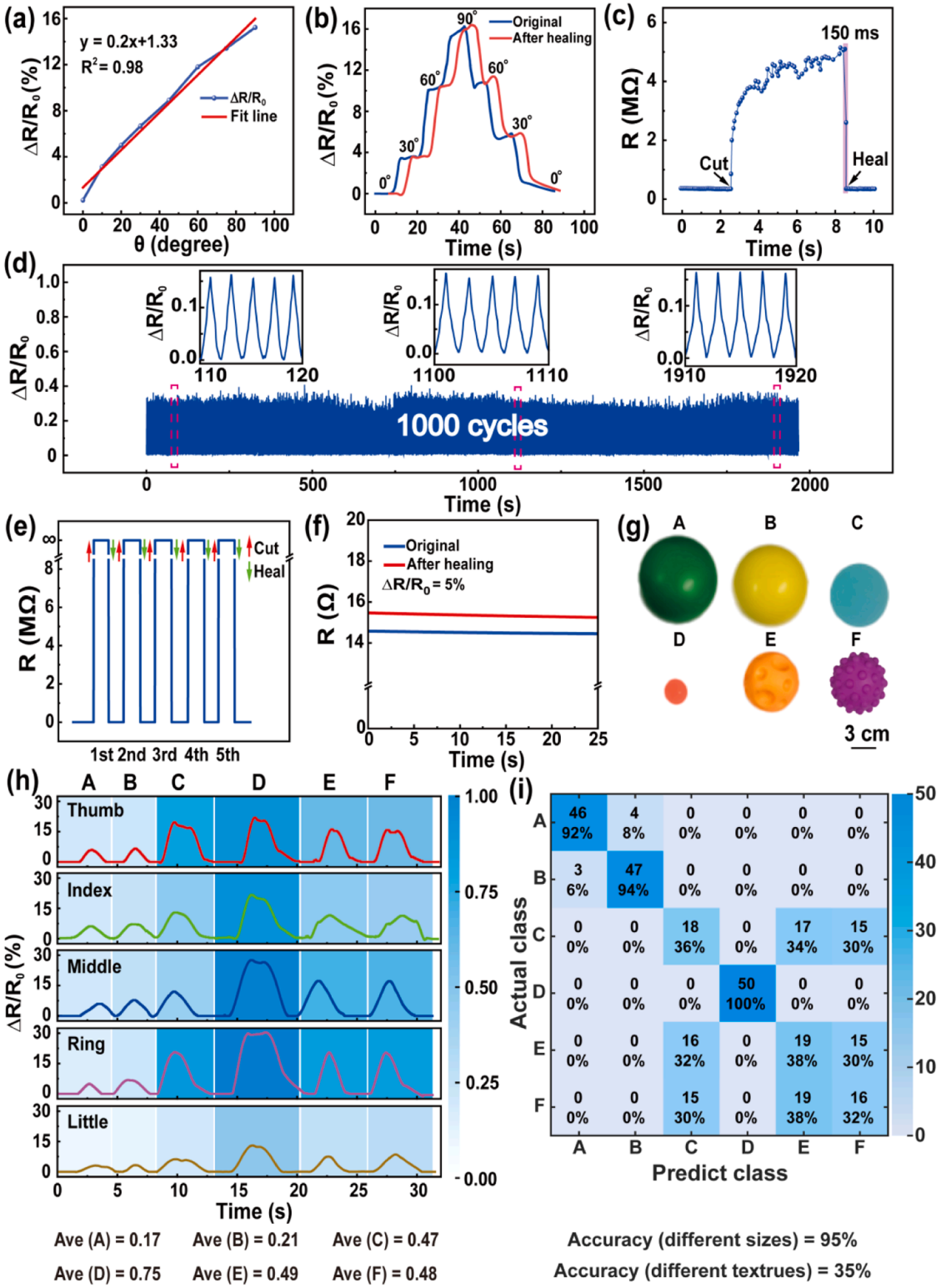

Fig. 3. Performance evaluation of a flexible self-healing piezoresistive sensor. (a) Sensitivity testing of the sensor. (b) Correlation between the bending angle and the rate of resistance change. (c) Recovery speed of electrical signals following damage to the piezoresistive sensor. (d) Repeatability assessment after 24 h of self-healing. (e) Durability evaluation over five cycles of cutting and self-healing. (f) Variation in initial resistance after five cycles of cutting and self-healing. (g) Six distinct pellets labeled A through F for testing. (h) The blue signal represented the magnitude of the resistance change rate. The sensors were attached to the five fingers of a volunteer, and the resistance change rate signals during the grasping of six different balls (A - F) were recorded. (i) Recognition rate matrix and accuracy of volunteers performing 50 grasping trials for each object as shown in (g).

and electrical stability tests, we further evaluated the sensor's performance under varying environmental conditions, including temperature and humidity fluctuation (Fig. S8). In these experiments, the sensor was subjected to a controlled chamber where both temperature and humidity were systematically varied. The results confirm the sensor's robustness, with minimal changes (approximately 5 %) in resistance

change rate at 90° bending angle when exposed to temperature fluctuations up to 60°C and humidity variations up to 76 %. These findings demonstrate that the sensor maintains reliable performance under fluctuating temperature and humidity conditions and exhibits effective recovery from damage. This ensures its suitability for practical applications in dynamic environments.

For the grasping experiments, five identical piezoresistive sensors with self-healing features were affixed to finger joints to evaluate six objects (A–F), including four small balls with smooth surfaces of varying diameters (d = 10 cm, 9 cm, 6 cm, and 2.5 cm) and two small balls (d = 6 cm) with differing surface roughness (Fig. 3g). The object recognition experiment was conducted using the STM32F103C8T6 single chip (STMicroelectronics) as the main control and signal analysis unit, with voltage divider circuits employed to detect the signals from the piezoresistive sensing layers (Fig. S9). Prior to formal testing, standard signal measurements were conducted to normalize piezoresistive responses across all objects. Each object was grasped 20 times, and the output peak values from each sensor channel were recorded. The peak values were then averaged to yield standardized signal values for each channel. To validate the feasibility of piezoresistive sensors for determining object size, the maximum resistance change recorded during grasping was used as a characteristic value and normalized. For normalization, the C-value in the CMYK color representation was mapped to the absolute resistance change rate, where smaller object sizes corresponded to higher C-values. Specifically, a resistance change rate of 0 % corresponded to a C-value of 0 %, while rates $\geq$ 30 % corresponded to a C-value of 100 %. These normalized values were transformed into intensity maps, with variations visually represented as color differences reflecting object size. Given that finger bending varied among the five fingers when grasping the same object, an average value (Ave) from all five sensors was calculated to synthesize a size estimate. During actual object recognition, the Ave value of each object was compared against its standard reference value, allowing numerical errors within ± 5 % to indicate successful recognition. The STM32F103C8T6 microcontroller processed the data and provided feedback on the accuracy of recognition. As shown in Fig. 3h, grasping larger-diameter balls results in reduced finger bending and smaller resistance changes, while smaller-diameter balls cause greater bending and larger resistance changes. The colored regions in Fig. 3h depict intensity maps of normalized signal peaks from the five sensors. The Ave value effectively reflects object size, with Ball A (d = 10 cm) yielding the smallest Ave (0.17) and Ball D (d = 2.5 cm) producing the largest Ave (0.75). Balls C, E, and F have similar Aves due to identical diameters, despite differences in surface roughness. Based on this method, 50 recognition experiments were conducted on the six objects, and the results were recorded in a recognition rate matrix (Fig. 3i). The piezoresistive sensors achieves a 95 % accuracy rate in distinguishing spheres of varying diameters. However, because Balls C, E, and F share the same diameter (6 cm), the piezoresistive sensor alone could not differentiate them based on surface roughness, resulting in an accuracy rate of 35 %.

3.3. Sensing performance of self-healing piezoelectric sensor

The contact force experienced by the finger varies due to the distinct surface morphology of each object, resulting in fluctuations in the output voltage of the flexible piezoelectric sensor. Upon contact with an object, the piezoelectric sensor generates an output voltage signal that is dependent on the surface morphology of the object. The fundamental characteristics of the piezoelectric sensing layer are illustrated in Fig. S10a, which presents a milky soft film. It is worth noting that if no modifications are made to the PZT particles during the preparation process of this film, noticeable agglomeration and uneven distribution will occur within H-PDMS as depicted in the zirconium element mapping in Fig. S10b. However, after modification, significant improvements are observed regarding PZT particle distribution within H-PDMS as confirmed by zirconium element mapping diagram (Fig. S10c). Furthermore, SEM image displays a relatively uniform distribution and micron-level size for modified PZT particles within the piezoelectric film (Fig. S10d). When the piezoelectric sensor is unpolarized, an extremely weak voltage signal is generated upon applying a pressure of 250 N. In contrast, after polarization treatment, the sensor produces a voltage signal approaching 4 V under identical pressure conditions (Fig. S11). This phenomenon occurs because the dipole orientations of PZT particles are initially random, leading to only partial deformation of the PZT lattices and consequently generating minimal charge. Following polarization, the dipole orientations within PZT become more aligned, enabling greater charge generation at the upper and lower electrodes under applied force, thereby producing a significantly stronger voltage signal [44–46]. Since the piezoelectric performance of the piezoelectric sensor relies on the PZT particles, it is crucial to consider their content and their impact on output performance. We investigated how varying PZT particle contents affect sensor output performance, as shown in Fig. S12, with the PZT content increasing from 30 wt% to 80 wt%, the output signal shows a trend of first increasing and then decreasing, reaching optimal levels at 60 wt%. Excessive PZT content diminishes both piezoelectric coefficient and permittivity of the composite material, leading to reduced capacitance and subsequent decrease in piezoelectric signal output.

The performance of the output electrical signal of the sensor was evaluated using the compression function of the universal testing machine. As the force applied to the piezoelectric sensing unit increases, the corresponding output voltage also increases (Fig. 4a). The peak voltage values obtained at different force levels are used as reference points to construct the sensitivity curve (Fig. 4b), which exhibits a two-segment linear relationship within the range of 0–50 N. The linearity (R^2) and sensitivity factor of piezoelectric sensor (*SFE)* are critical parameters for assessing sensor performance. *SFE* is defined as $SFE = (V\text{-}V_0)/\Delta F$ (V is the current voltage value of the sensor, V_0 is the chosen initial voltage value of the sensor, and ΔF is the pressure change of the sensor). During pressure tests within 0–20 N range, the sensor's voltage change exhibits an almost linear relationship (R^2 = 0.97) with the applied pressure, yielding a *SFE* of 0.035. In the higher pressure range of 20–50 N, the *SFE* decreases to 0.012. Furthermore, since the piezoelectric film of the piezoelectric sensor is composed of H-PDMS mixed with PZT particles, the self-healing mechanism of the piezoelectric sensor resembles that of H-PDMS. It requires 24 h to fully recover its mechanical properties at r.t. condition. Regarding the self-healing signal recovery ability of the sensor, due to the vertically arranged electrode structure, even if the sensor is damaged, the upper and lower electrodes remain intact, preserving the piezoelectric effect. However, damage to the piezoelectric film can lead to destruction of the gold electrodes on its surface, reducing charge accumulation on the plates under pressure, thereby decreasing the output voltage of the sensor (Fig. 4c). After 24 h of self-healing, the gold electrodes on the sensor's surface re-establish contact, allowing for resumed normal operation. However, due to residual cracks in the electrode, the sensor's output performance declines slightly. Specifically, the restored output voltage reaches 3.8 V, corresponding to a self-healing efficiency of 93 % compared to its original output of 4.1 V (Fig. 4c). Subsequently, we conducted pressure tests on these self-healed piezoelectric sensors for 1000 cycles under a load of 50 N using a data acquisition card; the results show excellent repeatability (Fig. 4d). To evaluate the sensor's durability under multiple damages, we performed cyclic cuts at the same position three times and observed a gradual decline in output after each cut and subsequent self-healing (Fig. 4e). After the third healing cycle, the signal output capacity decreases to approximately 76 % of the original state, demonstrating the sensor's repeatable self-healing capability. Similarly, the performance of the piezoelectric sensors was evaluated under varying temperature and humidity conditions (Fig. S13a). At a constant pressure of 50 N, the output signal decreases slightly with increasing temperature, dropping by only 6 % at 60°C (Fig. S13b). The output signal also decreases slightly with increasing humidity, dropping by about 5 % at 76 % relative

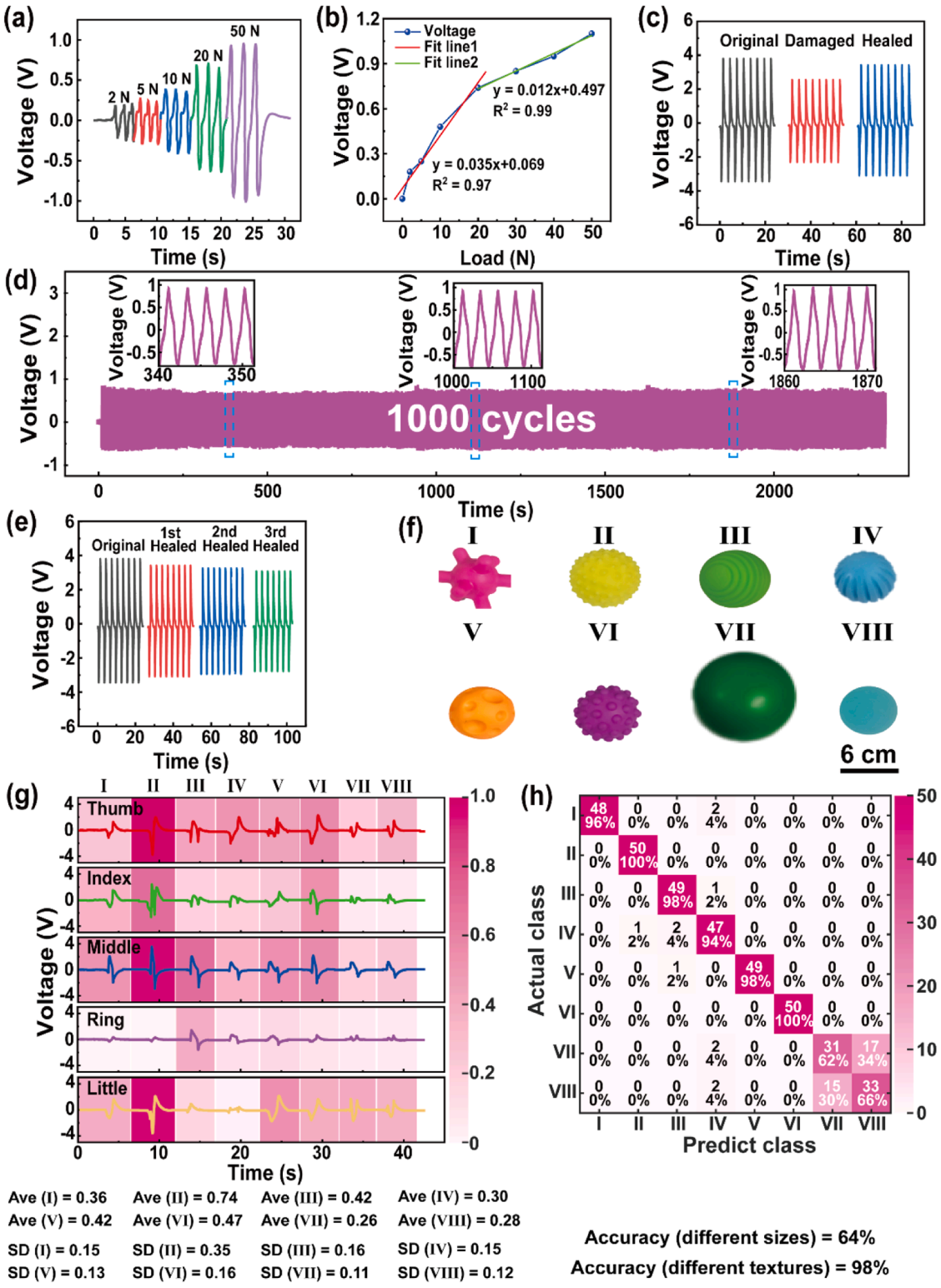

Fig. 4. Performance evaluation of the self-healing piezoelectric sensor. (a) Variations in output voltage under different pressure conditions. (b) Sensitivity analysis of the piezoelectric sensor. (c) Performance comparison of the piezoelectric sensor in its original state, post-damage, and post-self-healing. (d) Repeatability assessment of the sensor after 24 h of self-healing. (e) Performance changes following multiple cutting and self-healing cycles. (f) Eight distinct objects used for grasping tests (labeled I - VIII). (g) Pink shading indicated changes in the amplitude of the sensor's output voltage. The sensors were attached to all five fingers of a volunteer, and voltage changes during the grasping of six different balls (labeled I - VI) were recorded. (h) Recognition rate matrix and accuracy of volunteers performing 50 grasping trials for each object as described in (g).

humidity (Fig. S13c). These results indicate that variations in temperature and humidity have a negligible effect on the performance of piezoelectric sensors.

Given the excellent sensing sensitivity and self-healing properties of the self-healing piezoelectric sensors, five piezoelectric sensors were affixed to the fingertips of five fingers to carry out grasping experiments

on objects with varying levels of roughness (Fig. S15) to further evaluate the feasibility of these sensors for morphology recognition of object surfaces. The eight objects (labeled I-VIII in Fig. 4f) consist of six balls with varying surface textures (each with a diameter of 6 cm) and two smooth-surfaced balls (with diameters of 10 cm and 6 cm, respectively). The object recognition experiment was further performed by using a charge amplifier (TL064AD operational amplifier, Sungine), and the signal was detected by amplifying the output signal of the piezoelectric sensor using an STM32F103C8T6 microcontroller (Fig. S9). Similar to the identification experiment preparation of the piezoresistive sensor, a standard piezoelectric signal measurement experiment was conducted using the same circuit configuration. The piezoelectric sensors were worn to grasp each object 20 times, with the output peak signals recorded for each channel. These peak values were then averaged to establish the standardized signal value for each channel. The normalization process employed the CMYK representation, where the percentage change in the M-value reflected variations in the piezoelectric signal strength. Specifically, as the absolute value of the piezoelectric signal increased, the M-value percentage also increased, representing greater surface roughness. For instance, an output voltage of 0 V corresponded to an M-value of 0 %, while an output voltage peak $\geq$ 4 V corresponded to an M-value of 100 %. Based on this method, the CMYK standard values for each channel were recorded. To assess the piezoelectric sensor's ability to detect surface features, the mean value (Ave) was used to represent the overall surface curvature, while the standard deviation (SD) reflected the internal complexity of the surface topography. The Ave and SD values for eight test objects were recorded as standard references. During detection, the actual Ave and SD values were compared with the standard references with an allowable error margin of $\pm$ 5 %, allowing the microcontroller to match the results and determine recognition accuracy. When the sensor grasps a ball, it generates signals as depicted by the curve in Fig. 4g. Interestingly, even when using the same sensor, the signal exhibits both positive and negative values in both directions and varies among different spheres; moreover, for a given sphere, the output signals are different between sensors. These variations arise due to non-uniform curvatures on object surfaces that result in contact at different points during grasping. The color area shown in Fig. 4g represents the intensity maps of normalized signal peaks from these five piezoelectric sensors. The calculated Ave and SD values for each measured object were recorded in the lower panel, quantitatively reflecting the surface information of the measured object in the form of data. It could be observed that varying surface curvatures significantly influence the signal outputs from piezoelectric sensors, with increased surface curvature resulting in higher output signals [43]. Relevant diagrams and theoretical formulas are presented in Fig. S14. For instance, object II possesses the largest surface curvature, therefore leading to the largest output signal; while the smooth ball has minimal surface curvature and therefore the smallest output signal. According to the above test method, 50 grasp recognition experiments were conducted on eight objects (I-VIII), the corresponding recognition results were recorded, and the obtained recognition rate matrix was shown in Fig. 4h. The fabricated piezoelectric sensor demonstrates enhanced suitability for resolving the surface shape of the sphere, achieving an impressive accuracy of 98 % for different surfaces with similar sizes. However, recognition accuracy drops to 32 % for smooth spheres VII and VIII, which exhibits nearly identical curvatures. The experimental results demonstrate that the piezoelectric film composed of PZT and H-PDMS retains its piezoelectric properties even after damage. Specifically, the WHBs in H-PDMS play a critical role in quickly restoring the damaged sensor. Additionally, the SHBs enable the sensor to recover its mechanical properties and improve sensing capabilities within 24 h of self-healing. However, due to the irreversible damage to the gold electrodes upon initial damage, the sensor's performance exhibits a gradual decline after multiple damage events.

3.4. Dual-mode tactile sensing strategy for object recognition

Single-mode sensors have their own advantages and disadvantages in object recognition. Piezoresistive sensors can only recognize the size of an object, while piezoelectric sensors can only determine the surface contour of the object. Therefore, combining these two types of sensors enables more accurate object recognition. In our experiments, we selected three objects (No. 1: d=10 cm, smooth; No. 2: d=6 cm, smooth; No. 3: d=6 cm, rough) that cannot be well recognized by a single sensor. We analyzed and normalized the signals captured from both the piezoresistive (R) and piezoelectric (E) sensing layers. For the accuracy recognition of dual-mode signals, it is also necessary to normalize the piezoresistive and piezoelectric signals respectively, and then superimpose the values of each proportion of the two CMYK color blocks to form a single new color block. Similar to the standard signal determination experiment of the independent sensing layer, the CMYK color block standard value of the measured object is established. In the actual object recognition experiment, if the error of each ratio value of CMYK detected and each ratio value of standard CMYK is within $\pm$ 5 %, the recognition is successful. The two signals from the dual-mode sensing system (D) were combined to obtain a color-coded representation via the CMKY color symbols (Fig. 5a). This coupled signal block provides better discrimination compared to using a single sensor alone. In machine recognition, an object can be distinguished based on this color block after coupling with reference to a standard image (Fig. S15). As illustrated in Fig. S15, the x-axis denotes the proportion of the C-Value in the CMYK color model, where an increase corresponds to smaller object sizes. The y-axis indicates the M-Value proportion, with higher values reflecting increased surface roughness. This means that objects with rougher surfaces (larger surface curvature) are located higher above the chromaticity diagram, while objects with smaller sizes are positioned further to the right of the standard image. The combination of the piezoresistive sensor and piezoelectric sensor not only allows for recognizing objects of different sizes but also enables distinguishing between objects with varying surface morphology, achieving a recognition rate of 96 % (Fig. 5b). In order to verify the recognition accuracy of the dual-mode sensing system, the two sensors are cut under the r.t. conditions. After 24 h of self-healing and subsequent object recognition experiment, the recognition rate still remains at 96 %. Moreover, a comprehensive comparison is performed between our sensing system and other sensors reported in the literature [47–54] that featured self-healing and sensing recognition capabilities (Fig. 5c). The results highlight the superiority of our sensing system across multiple dimensions, including sensing modalities, self-healing time, self-healing efficiency, mechanical properties before and after self-healing, and electrical signal recovery during self-healing events.

To investigate the influence of sensor deployment positions on dual-mode sensing performance, comparative experiments were conducted by placing the sensors at different positions on mechanical claws. When mounted on the outer surface of the mechanical claw (Fig. S16a), the piezoresistive sensor effectively distinguishes fruit size (Fig. S16b) but fails to detect surface roughness. Conversely, the piezoelectric sensor mounted on the outer surface exhibits weak signals with significant spurious peaks (Fig. S16c) due to insufficient direct contact with the fruit, making surface roughness detection ineffective. When the sensors were mounted on the inner side of the mechanical claw in direct contact with the fruit (Fig. S16d), the piezoresistive sensor could not detect the bending angle of the claw, making it unsuitable for fruit size determination (Fig. S16e). However, the piezoelectric sensor successfully detects surface roughness but fails to distinguish fruit size (Fig. S16f). Therefore, to achieve optimal dual-mode sensing performance while minimizing damage from litchi thorns, the piezoresistive sensor is mounted on the lateral bending mechanism on the outer side of the claw, and the piezoelectric sensor is positioned on the inner side (Fig. 5d).

As an application demonstration, the integration of these sensors with a mechanical claw is anticipated to be employed in the lychee

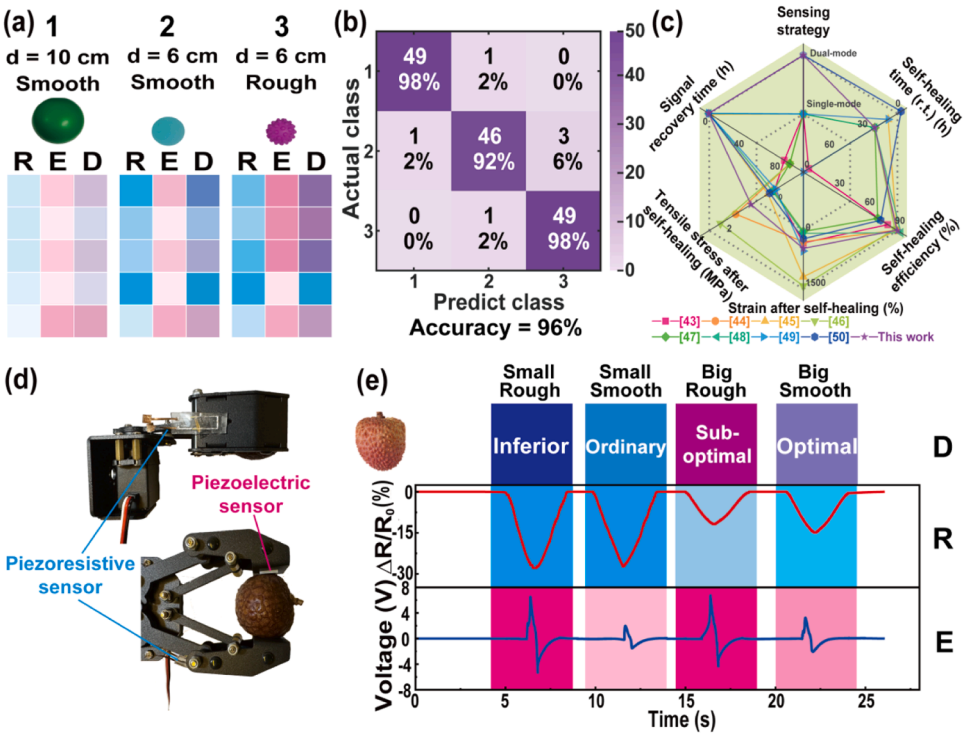

Fig. 5. Object recognition and detection application of self-healing sensors for dual-mode sensing. (a) Two sensing color-block signals and mixed CMYK color-block signals obtained when three objects were grasped by wearing the sensors. (b) Matrix of recognition rates of three objects. (c) Comparison graph of this work with other self-repairing sensors. (d) Detecting the quality of lychee using a mechanical claw with fully self-healing dual-mode tactile sensing system. (e) Electrical signal for detecting the quality of lychee.

tactile inspection for grading the quality of lychee. The dual-mode sensing strategy enables differentiation based on lychee size and surface roughness. For the normalization of lychee quality detection, adjustments are essential to account for the variations in size and surface characteristics between lychees and small spheres. Specifically, for the piezoresistive sensor, when the absolute value of the resistance change rate is 0 %, the corresponding C-value percentage is set to 0 %, and when the absolute value of the resistance change rate reaches or exceeds 32 %, the C-value percentage is set to 100 %. Similarly, for the piezoelectric sensor, an output voltage of 0 V corresponds to an M-value percentage of 0 %, while an output voltage peak of 7.5 V or higher corresponds to an M-value percentage of 100 %. By analyzing the sensing signals, lychee quality is effectively classified based on the depth of CMYK color blocks (Fig. 5e). Thus, the quality of lychees can be graded based on size and peel roughness, using the criteria outlined in Table S1. The exceptional self-healing properties of the dual-mode sensing system further enhance its durability, making it suitable for practical applications in object recognition and automated fruit sorting using robotic systems.

4. Conclusion

Inspired by the self-healing mechanism of human fingers and their tactile sensing process in object recognition, we have developed two types of sensors with inherent self-healing capability and dual-mode sensing strategy for precise object recognition and classification. The piezoresistive sensor is a composed of H-PDMS and liquid metal ink, enabling the creation of a highly linear and accurate detection of an object's size through finger joint bending. Additionally, the piezoelectric sensor incorporated with PZT particles in H-PDMS effectively captures surface topography information of an object by detecting the contact force exerted by a finger. By integrating the two sensing modes and employing a CMYK color block overlay to visually represent both size and surface information of the detected object, the recognition rate of the sensing system can reach 96 %. The dual-mode sensing system uses functional self-healing H-PDMS material as the base material of the sensor, exhibiting remarkable self-healing properties akin to human skin, demonstrating an outstanding self-healing efficiency in mechanical property, reaching 93 % after a 24-h healing period at room temperature. Additionally, the electrical signal recovery efficiencies for the piezoresistive and piezoelectric sensors are 95 % and 93 %, respectively. The exciting self-repairing capability attribute to two types of hydrogen bonds with different strength and recombination ability, namely SHBs with quadruple hydrogen bonding provide excellent elasticity, while WHBs effectively dissipate strain during deformation. As a demonstration, the fully self-healing dual-mode sensing system can classify lychee fruit quality into four distinct grades: optimal, sub-optimal, ordinary, and inferior. This highlights their significant potential for intelligent sorting systems in fruit quality assessment.

CRediT authorship contribution statement

Xuanzi Luo: Investigation, Simulation, Data curation, Formal analysis, Writing – original draft preparation. **Xin Zhang**: Conceptualization, Methodology, Software, Investigation. **Shanpeng Ji**: Investigation, Validation. **Chao Wu**: Investigation. **Lin Cheng**: Supervision, Project administration, Writing – original draft preparation. **Daoyou Guo**: Investigation. **Shunli Wang**: Investigation. **Huaping Wu**: Investigation, Methodology, Conceptualization. **Aiping Liu**: Supervision, Funding acquisition, Project administration, Writing – review & editing.

Declaration of Competing Interest

The authors declare that they have no known competing financial interests or personal relationships that could have appeared to influence the work reported in this paper.

Acknowledgements

This work was supported by the National Natural Science Foundation of China (No. 12272351, 62401509 and 12372168), the National Key Research and Development Program of China (2024YFB3816500), the Zhejiang Provincial Natural Science Foundation of China (No. LZ24A020004 and LRG25A020001), the Youth Top-notch Talent Project of Zhejiang Ten Thousand Plan of China (No. ZJWR0308010), and the "Pioneer" and "Leading Goose" R&D Program of Zhejiang (Grant no. 2023C01051).

Appendix A. Supporting information

Supplementary data associated with this article can be found in the online version at doi:10.1016/j.nanoen.2025.110757.

Data Availability

Data will be made available on request.

References

[1] M. Zhu, Z. Sun, Z. Zhang, Q. Shi, T. He, H. Liu, et al., Haptic-feedback smart glove as a creative human-machine interface (HMI) for virtual/augmented reality applications, Sci. Adv. 6 (2020) eaaz8693, https://doi.org/10.1126/sciadv.aaz8693.
[2] X. Zeng, Y. Hu, Sensation and perception of a bioinspired flexible smart sensor system, ACS Nano (6) (2021) 9238–9243, https://doi.org/10.1021/acsnano.1c03408.
[3] J. Zhang, H. Yao, J. Mo, S. Chen, Y. Xie, S. Ma, et al., Finger-inspired rigid-soft hybrid tactile sensor with superior sensitivity at high frequency, Nat. Commun. 13 (2022) 5076, https://doi.org/10.1038/s41467-022-32827-7.
[4] R. Young, A general architecture for robotics systems: A perception-based approach to artificial life, Artif. Life. 23 (2017) 236–286, https://doi.org/10.1162/ARTL_a_00229.
[5] H. Sun, K.J. Kuchenbecker, G. Martius, A soft thumb-sized vision-based sensor with accurate all-round force perception, Nat. Mach. Intell. 4 (2022) 135–145, https://doi.org/10.1038/s42256-021-00439-3.
[6] W. Yuan, S. Dong, E.H. Adelson, GelSight: high-resolution robot tactile sensors for estimating geometry and force, Sensors 17 (2017) 2762, https://doi.org/10.3390/s17122762.
[7] M. Zhu, T. He, C. Lee, Technologies toward next generation human machine interfaces: From machine learning enhanced tactile sensing to neuromorphic sensory systems, Appl. Phys. Rev. 7 (2020) 031305, https://doi.org/10.1063/5.0016485.
[8] R. Krishnamurthy, J. Cecil, A next-generation IoT-based collaborative framework for electronics assembly, Int. J. Adv. Manuf. Technol. 96 (2018) 39–52, https://doi.org/10.1007/s00170-017-1561-x.
[9] S. Li, et al., M3Tac: A multispectral multimodal visuotactile sensor with beyond-human sensory capabilities, IEEE Trans. Robot. 40 (2024) 4506–4525, https://doi.org/10.1109/TRO.2024.3462931.
[10] S. Mu, S. Li, H. Zhao, Z. Wang, X. Xiao, X. Xiao, et al., A platypus-inspired electro-mechanosensory finger for remote control and tactile sensing, Nano Energy 116 (2023) 108790, https://doi.org/10.1016/j.nanoen.2023.108790.
[11] S. Lee, Q. Shi, C. Lee, From flexible electronics technology in the era of IoT and artificial intelligence toward future implanted body sensor networks, APL Mater. 7 (2019) 031302, https://doi.org/10.1063/1.5063498.
[12] D. Ruan, G. Chen, X. Luo, L. Cheng, H. Wu, A. Liu, Bionic octopus-like flexible three-dimensional force sensor for meticulous handwriting recognition in human-computer interactions, Nano Energy 123 (2024) 109357, https://doi.org/10.1016/j.nanoen.2024.109357.
[13] H. Zhang, H. Li, Y. Li, Biomimetic electronic skin for robots aiming at superior dynamic-static perception and material cognition based on triboelectric-piezoresistive effects, Nano Lett. 24 (2024) 4002–4011, https://doi.org/10.1021/acs.nanolett.4c00623.
[14] Y. Tang, Q. Dang, W. Zhang, H. Guo, H. Pan, Y. Xiang, et al., Synchronous monitoring of underwater dynamic/static pressure based on piezoelectric/capacitive polyester elastomer/carbon nanotube composites, J. Mater. Chem. A. 12 (2024) 18089–18095, https://doi.org/10.1039/D4TA02298J.
[15] Y. Qiu, Z. Wang, P. Zhu, B. Su, C. Wei, Y. Tian, et al., A multisensory-feedback tactile glove with dense coverage of sensing arrays for object recognition, Chem. Eng. J. 455 (2023) 140890, https://doi.org/10.1016/j.cej.2022.140890.
[16] G. Kalimuldina, N. Turdakyn, I. Abay, A. Medeubayev, A. Nurpeissova, D. Adair, et al., A review of piezoelectric PVDF film by electrospinning and its applications, Sensors 20 (2020) 5214, https://doi.org/10.3390/s20185214.
[17] Y. Qiu, C. Wang, X. Lu, H. Wu, X. Ma, J. Hu, et al., A biomimetic Drosera capensis with adaptive decision-predation behavior based on multifunctional sensing and fast actuating capability, Adv. Funct. Mater. 32 (2021) 2110296, https://doi.org/10.1002/adfm.202110296.
[18] Q. Zhai, S. Gong, Y. Wang, Q. Lyu, Y. Liu, Y. Ling, et al., Enokitake mushroom-like standing gold nanowires toward wearable noninvasive bimodal glucose and strain sensing, ACS Appl. Mater. Interfaces 11 (2019) 9724–9729, https://doi.org/10.1021/acsami.8b19383.
[19] Y. Wang, S. Gong, D. Gomez, Y. Ling, L.W. Yap, G.P. Simon, et al., Unconventional janus properties of enokitake-like gold nanowire films, ACS Nano 12 (2018) 8717–8722, https://doi.org/10.1021/acsnano.8b04748.
[20] Y. Qiu, Y. Tian, S. Sun, J. Hu, Y. Wang, Z. Zhang, et al., Bioinspired, multifunctional dual-mode pressure sensors as electronic skin for decoding complex loading processes and human motions, Nano Energy 78 (2020) 105337, https://doi.org/10.1016/j.nanoen.2020.105337.
[21] Y. Qiu, F. Wang, Z. Zhang, K. Shi, Y. Song, J. Lu, et al., Quantitative softness and texture bimodal haptic sensors for robotic clinical feature identification and intelligent picking, Sci. Adv. 10 (2024) eadp0348, https://doi.org/10.1126/sciadv.adp0348.
[22] Y. Liu, J. Tao, Y. Mo, R. Bao, C. Pan, Ultrasensitive touch sensor for simultaneous tactile and slip sensing, Adv. Mater. 36 (2024) 2313857, https://doi.org/10.1002/adma.202313857.
[23] S. Li, S. Chen, L. Yang, Y. Guo, K. Tan, S. Liu, et al., Bimodal capacitive tactile sensor assisted by shield effect of triboelectric nanogenerator, Nano Energy 118 (2023) 108946, https://doi.org/10.1016/j.nanoen.2023.108946.
[24] Y. Ji, S. Yin, Y. Liu, C.R. Bowen, Y. Yang, Dual-mode temperature sensor based on ferroelectric Bi0.5Na0.5TiO3 materials for robotic tactile perception, Nano Energy 128 (2024) 109982, https://doi.org/10.1016/j.nanoen.2024.109982.
[25] A. Chortos, J. Liu, Z. Bao, Pursuing prosthetic electronic skin, Nat. Mater. 15 (2016) 937–950, https://doi.org/10.1038/nmat4671.
[26] D. He, W. Li, R. Yuan, F. Xin, C. Stefanini, Preliminary study on piezoresistive and piezoelectric properties of a double-layer soft material for tactile sensing, Mater. Sci. 21 (2015) 238–243, https://doi.org/10.5755/j01.ms.21.2.6454.
[27] Z. Gao, B. Ren, Z. Fang, H. Kang, J. Han, J. Li, Accurate recognition of object contour based on flexible piezoelectric and piezoresistive dual mode strain sensors, Sens. Actuator A Phys. 332 (2021) 113121, https://doi.org/10.1016/j.sna.2021.113121.
[28] G. Lee, J.H. Son, S. Lee, S.W. Kim, D. Kim, N.N. Nguyen, et al., Fingerpad-inspired multimodal electronic skin for material discrimination and texture recognition, Adv. Sci. 8 (2021) 2002606, https://doi.org/10.1002/advs.202002606.
[29] J. Sun, X. Pu, M. Liu, A. Yu, C. Du, J. Zhai, et al., Self-healable, stretchable, transparent Triboelectric nanogenerators as soft power sources, ACS Nano 12 (2018) 6147–6155, https://doi.org/10.1021/acsnano.8b02479.
[30] S. Wang, J. Xu, W. Wang, G.N. Wang, R. Rastak, F. Molina-Lopez, et al., Skin electronics from scalable fabrication of an intrinsically stretchable transistor array, Nature 555 (2018) 83–88, https://doi.org/10.1038/nature25494.
[31] M. Park, W. Yang, J.W. Kim, Y. Choi, S. Kim, Y. Lee, et al., A fully self-healing patch of integrated bio-signal monitoring sensors with self-healing microporous foam and au nanosheet electrodes, Adv. Funct. Mater. 34 (2024) 2402508, https://doi.org/10.1002/adfm.202402508.
[32] Y. Zheng, R. Yin, Y. Zhao, H. Liu, D. Zhang, X. Shi, et al., Conductive MXene/cotton fabric based pressure sensor with both high sensitivity and wide sensing range for human motion detection and E-skin, Chem. Eng. J. 420 (2021) 127720, https://doi.org/10.1016/j.cej.2020.127720.
[33] L.M. Li, X.F. Ji, K. Chen, Conductive, self-healing, and antibacterial Ag/MXene-PVA hydrogel as wearable skin-like sensors, J. Biomater. Appl. 37 (2021) 1169–1181, https://doi.org/10.1177/08853282221131137.
[34] X. Shi, K. Zhang, L. Zhao, B. Jiang, Y. Huang, Robust, self-healable siloxane elastomers constructed by multiple dynamic bonds for stretchable electronics and microsystems, Ind. Eng. Chem. Res. 60 (2021) 2154–2162, https://doi.org/10.1021/acs.iecr.0c05238.
[35] J. Kang, D. Son, G.-J.N. Wang, Y. Liu, J. Lopez, Y. Kim, et al., Tough and water-insensitive self-healing elastomer for robust electronic skin, Adv. Mater. 30 (2018) 1706846, https://doi.org/10.1002/adma.201706846.
[36] X. Dai, Q. Liang, Z. Zhao, Y. Wu, J. Yang, J. Han, et al., Self-powered sensors for flexible electronic skins capable of self-healing under multiple extreme environments, Nano Energy 121 (2024) 109238, https://doi.org/10.1016/j.nanoen.2023.109239.
[37] X. Xun, Z. Zhang, X. Zhao, B. Zhao, F. Gao, Z. Kang, et al., Highly robust and self-powered electronic skin based on tough conductive self-healing elastomer, ACS Nano 14 (2020) 9066–9072, https://doi.org/10.1021/acsnano.0c04158.
[38] O.A. Peña, P. Martin, Cellular and molecular mechanisms of skin wound healing, Nat. Rev. Mol. Cell Biol. 25 (2024) 599–616, https://doi.org/10.1038/s41580-024-00715-1.
[39] K. Sahre, M.H.A. Elrehim, K.-J. Eichhorn, B. Voit, Monitoring of the synthesis of hyperbranched poly(urea-urethane)s by real-time attenuated total reflection (ATR)-FT-IR spectroscopy, Macromol. Mater. Eng. 291 (2006) 470–476, https://doi.org/10.1002/mame.200500358.
[40] Z. Yang, H. Li, L. Zhang, X. Lai, X. Zeng, Highly stretchable, transparent and room-temperature self-healable polydimethylsiloxane elastomer for bending sensor, J. Colloid Interface Sci. 570 (2020) 1–10, https://doi.org/10.1016/j.jcis.2020.02.107.
[41] W. Bai, Z. Jiang, A.E. Ribbe, S. Thayumanavan, Smart organic two-dimensional materials based on a rational combination of non-covalent interactions, Angew. Chem. Int. Ed. 55 (2016) 10707, https://doi.org/10.1002/anie.201605050.
[42] J. Wu, Z. Wu, X. Lu, S. Han, B.R. Yang, X. Gui, et al., Ultrastretchable and stable strain sensors based on antifreezing and self-healing ionic organohydrogels for human motion monitoring, ACS Appl. Mater. Interfaces 11 (2019) 9405–9414, https://doi.org/10.1021/acsami.8b20267.

[43] X. Chen, P. Sun, H. Tian, X. Li, C. Wang, J. Duan, et al., Self-healing and stretchable conductor based on embedded liquid metal patterns within imprintable dynamic covalent elastomer, J. Mater. Chem. C 10 (2022) 1039–1047, https://doi.org/10.1039/D1TC05087G.
[44] S. Kong, C. Hong, W. Zhang, Y. Liu, Z. Wang, X. Yang, et al., Performance enhancement of soft-PZT5 piezoelectric ceramics using poling technique, J. Am. Ceram. Soc. 105 (2022) 4744–4750, https://doi.org/10.1111/jace.18433.
[45] L. Lai, B. Li, S. Tian, Z. Zhao, S. Zhang, Y. Dai, Giant electrostrain in lead-free textured piezoceramics by defect dipole design, Adv. Mater. 35 (2023) 2300519, https://doi.org/10.1002/adma.202300519.
[46] J. Zhao, Z. You, A shoe-embedded piezoelectric energy harvester for wearable sensors, Sensors 14 (2014) 12497–12510, https://doi.org/10.3390/s140712497.
[47] Z. Li, Y. Shan, X. Wang, H. Li, K. Yang, Y. Cui, Self-healing flexible sensor based on metal-ligand coordination, Chem. Eng. J. 394 (2020) 124932, https://doi.org/10.1016/j.cej.2020.124932.
[48] Z. Ma, Z. Liu, J. Zou, H.-Y. Mi, Y. Liu, X. Jing, Self-healable and robust silicone elastomer for ultrasensitive flexible sensors, ACS Sustain. Chem. Eng. 11 (2023) 10496–10508, https://doi.org/10.1021/acssuschemeng.3c02168.
[49] S. Liu, O. Oderinde, I. Hussain, F. Yao, G. Fu, Dual ionic cross-linked double network hydrogel with self-healing, conductive, and force sensitive properties, Polymer 144 (2018) 111–120, https://doi.org/10.1016/j.polymer.2018.01.046.
[50] Z. Wang, Y. Liu, D. Zhang, C. Gao, Y. Wu, Mussel-inspired self-healing PDMS/AgNPs conductive elastomer with tunable mechanical properties and efficient antibacterial performances for wearable sensor, Compos. B. Eng. 224 (2021) 109213, https://doi.org/10.1016/j.compositesb.2021.109213.
[51] H. Du, N. Zhang, J. Wang, F. You, Simple preparation of redox induced shape memory and self-healable ionic liquid based gels for flexible strain sensors, Colloids Surf. A 671 (2023) 131633, https://doi.org/10.1016/j.colsurfa.2023.131633.
[52] X. Zhou, X. Zhang, H. Zhao, B.P. Krishnan, J. Cui, Self-healable and recyclable tactile force sensors with post-tunable sensitivity, Adv. Funct. Mater. 30 (2020) 2003533, https://doi.org/10.1002/adfm.202003533.
[53] M. Yang, J. Liu, D. Liu, J. Jiao, N. Cui, S. Liu, et al., A fully self-healing piezoelectric nanogenerator for self-powered pressure sensing electronic skin, Research (2021), https://doi.org/10.34133/2021/9793458.
[54] Y. Qiao, Q. Zhang, Y. Xiang, Z. Wang, X. Hu, Stretchable and self-healing electronic skin based on a piezoelectric/triboelectric polyester elastomer for deep and superficial sensation, J. Mater. Chem. A. 11 (2023) 20120–20128, https://doi.org/10.1039/D3TA03868H.

Xuanzi Luo received his B. E. degree in Guangdong Polytechnic Normal University in 2022. He is now studying for Master's degree in Zhejiang Sci-Tech University. His research interests involve solving multidimensional force perception problems in flexible tactile sensors with dual mode.

Xin Zhang received her B. E. degree in North University of China in 2023. She is now studying for Master's degree in Zhejiang Sci-Tech University. Her research interests are flexible proximity and tactile three-dimensional sensors.

Shanpeng Ji received his B. S. degree in Zhejiang Sci-Tech University of China in 2020. He had finished his Master course in 2023 and gained Master's degree in Zhejiang Sci-Tech University. His research interests are self-healing materials and tactile sensors.

Chao Wu received his Ph.D. degree in Materials Science from Zhejiang Sci-Tech University in 2022. He is currently an Associate Professor in the Department of Physics at Zhejiang Sci-Tech University. His research mainly focuses on smart optoelectronic sensing devices, wide-bandgap semiconductor materials, and smart fibers.

Lin Cheng received her Ph.D. degree in Materials Science and Engineering from the Zhejiang Sci-Tech University in 2023 and a Bachelor's degree from Henan University in 2017. Since 2017 her has been working at the Department of Physics (Zhejiang Sci-Tech University), where her research mainly focuses on flexible sensors based on smart materials/structures and their applications in human-computer interaction.

Daoyou Guo received his Ph.D. degree from Beijing University of Posts and Telecommunications in 2016. He is currently a Professor in the Department of Physics at Zhejiang Sci-Tech University. His research mainly focuses on condensed matter physics, wide-bandgap semiconductor materials, semiconductor devices, and wearable sensors.

Shunli Wang received his Ph.D. degree from Zhejiang Sci-Tech University in 2019. He is currently a Professor in the Department of Physics at Zhejiang Sci-Tech University. His research mainly focuses on wide-bandgap semiconductor materials, optoelectronic sensors, and wearable sensors.

Prof. Huaping Wu received his Ph. D. degree in Engineering Mechanics from the Harbin Institute of Technology in 2009 and a Bachelor's degree from the Harbin Institute of Technology in 2002. He worked as a visiting scholar at the Kyoto University in 2014 and a postdoctoral research fellow at the City University of Hong Kong in 2012. He is currently a Professor in the School of Mechanical Engineering at Zhejiang University of Technology. His research mainly focuses on the mechanics of smart materials/structures, bionic machinery and bionic manufacturing, and flexible electronics devices.

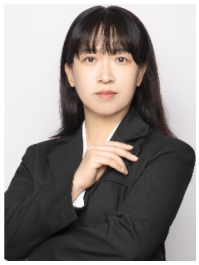

Prof. Aiping Liu received her Ph. D. degree in Material Science from the Harbin Institute of Technology in 2008. She worked as a postdoctoral research fellow at the Nanyang Technological University from 2009 to 2011 and a visiting scholar at the University of Texas at Austin from 2019 to 2020. She is currently a Professor in the Department of Physics at Zhejiang Sci-Tech University. Her research mainly focuses on functional inorganic/organic materials for wearable physical/chemical sensors and smart actuators.